EUV measurements of Kr XXI–Kr XXXIV and the effect of a magnetic-dipole line on allowed transitions

View the article online for updates and enhancements.

EUV measurements of Kr XXI–Kr XXXIV and the effect of a magnetic-dipole line on allowed transitions

Y A Podpaly, J D Gillaspy, J Reader and Yu Ralchenko

National Institute of Standards and Technology, Gaithersburg, MD 20899, USA

E-mail: yuri.podpaly@nist.gov

Abstract

We observed and analysed the extreme-ultraviolet spectra of highly charged ions of Kr XXI–Kr XXXIV produced in an electron beam ion trap (EBIT). The beam energies varied between 1.1 and 30 keV, and the wavelengths were observed between 3 and 17.3 nm with uncertainties of $\sim$0.003 nm. Six new lines were identified, and wavelength uncertainties have been improved for twelve additional transitions. It was found that a line intensity ratio for allowed transitions $3s^2 3p$–$3s^2 3d$ in Al-like Kr XXIV strongly deviated from predictions based on statistical weighting of the excited levels. Collisional-radiative modelling showed that this effect, which is due to the magnetic-dipole transition within the ground configuration $3s^2 3p$, offers sensitive diagnostics of electron density in the regime of interest to fusion tokamaks, EBITs, and other low-density plasmas.

Keywords: atomic physics, EUV spectroscopy, plasma diagnostics, highly charged ions, electron beam ion trap, krypton

(Some figures may appear in colour only in the online journal)

1. Introduction

Atomic spectra from ions in the electron temperature regimes applicable to fusion reactors are of particular interest for power balance and plasma diagnostic purposes. Emission lines can be used to identify the impurities in a plasma, and the line intensity ratios can be used to infer a variety of plasma parameters, such as electron density, temperature, and neutral particle density. Krypton has been used in tokamaks and is under consideration as a diagnostic element for the ITER tokamak [1], now under construction. Krypton's ionization potentials are such that helium-like krypton will be the dominant ionization stage in the core of ITER, so ion temperature and rotation velocity of the core plasma can be deduced from the helium-like resonance and satellite lines in the x-ray region. Krypton, iron, argon, and tungsten have been considered as diagnostic elements for the x-ray imaging spectrometer system on the ITER device [2, 3], with tungsten being the most recently considered element.

Krypton emissions have been studied extensively. For example, x-ray spectroscopy has been performed at the Lawrence Livermore National Laboratory (LLNL) and the National Institute of Standards and Technology (NIST) electron beam ion traps (EBITs) [4–6] and the GANIL accelerator [7]. Extreme ultraviolet (EUV) and x-ray transitions of krypton have also been studied on a variety of devices, such as the JET tokamak [8], the PITHON relativistic electron beam [9], EBITs [6, 10], and beam foil machines [11]. Highly ionized krypton in the visible range has been studied on the LHD stellarator [12] and the NIST and LLNL EBITs [13, 14]. A summary of krypton transitions and energy levels is listed in a 2007 comprehensive review by Saloman in [15].

In the present paper, spectra of highly charged krypton in the 3 to 17.3 nm region are observed at an EBIT device. The goal of this work is to identify spectral lines, to improve wavelength measurements for known lines, and to explore new spectroscopic techniques for plasma diagnostics.

2. Experiment

The measurements were performed at the NIST EBIT [16]. The EBIT electron beam can be tuned, by adjusting voltage, current, and time between trap dumps, to maximize the
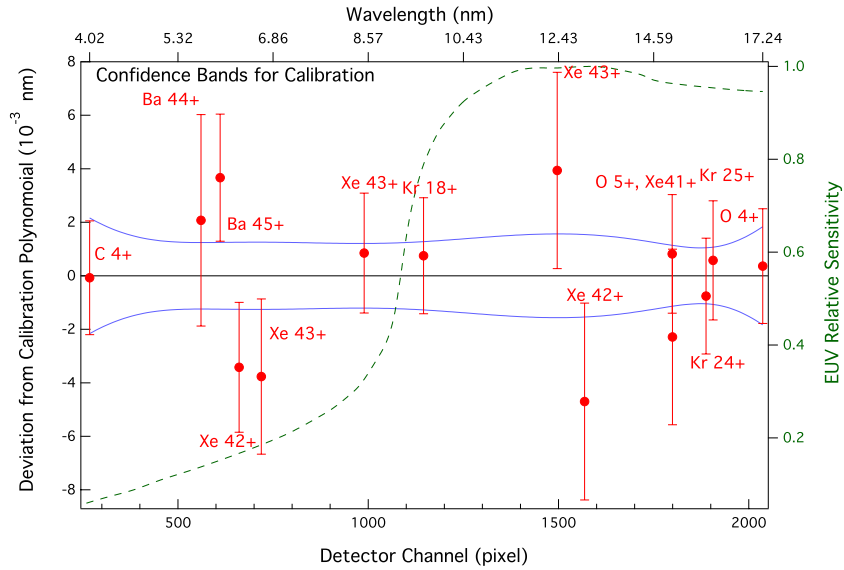
Figure 1. Residuals of the calibration points are shown along with their uncertainties. One standard deviation confidence interval (in blue) for the experimental calibration curve. Systematic uncertainty, 0.0021 nm, was added to the error bars to yield $\chi^2 \approx 10$. The EUV spectrometer approximate relative sensitivity is shown as the dashed line (right axis) which is taken from calculations reported in [17].

population of an ionization stage. The elements are selected via the use of a gas injector system. Beam tuning is confirmed by observing the output of a wide-band high-purity germanium detector that is operated simultaneously with the EUV observations. The ionized atoms are trapped electrostatically by the electron beam and via the use of two end-drift tubes at 500 and 220 V; the voltage asymmetry prevents ions from escaping towards the electron gun. A 2.8 T axial magnetic field is applied by a superconducting magnet. The measured EUV spectra were recorded with a 2048 pixel × 512 pixel (13.5 μm x 13.5 μm pixel dimensions) charge-coupled device (CCD) camera. The spectrometer has a 4 cm × 10 cm spherical gold-coated mirror ($R_c = 917.1 \pm 2.3$ cm) collecting light onto slit, behind which is a flat-field variable-spacing grating (3 cm × 5 cm, ~1200 lines mm^{-1}, $R_c = 564.9$ cm $\pm$ 2.0). The resolving power of this device is ~400, and the spectrometer is described in detail in [17]. Krypton was introduced to the EBIT via the gas injection system, while the electron beam energies were varied from 1.1 to 30 keV. The data were collected with multiple one-minute exposures of the EUV spectrometer. The detector pixels in the direction perpendicular to the dispersion plane were hardware-binned prior to readout to reduce noise. Filtering software was used to remove all points outside of five times the shot noise from the average counts per frame, removing spurious signals from cosmic rays and aberrant electronic noise.

The recorded spectra were calibrated using known lines of elements either introduced to the EBIT externally or available as intrinsic impurities. Spectral lines of carbon, oxygen, and xenon were observed via CO_2 and Xe gas injection; CO_2 was measured at 2.0 keV electron beam energy, and Xe was measured at 5.8 keV. We also made use of several lines of barium, which is a common dopant for electron guns, at 5.8 keV beam energy. Some previously known accurately measured lines from krypton could be utilized for calibration as well. Kr lines were used only if they were unblended, reliably

identified, and had published uncertainties below 0.001 nm. Three lines were selected with these properties, namely, a Kr^{24+} line at 15.8181 $\pm$ 0.0005 nm [18], a Kr^{18+} line at 9.6232 $\pm$ 0.0005 nm [19], and a Kr^{25+} line at 15.992 $\pm$ 0.0007 nm [20]. Our measurements of the wavelengths of these transitions using only the other calibration lines were 15.8187 $\pm$ 0.0035 nm, 9.6220 $\pm$ 0.0036 nm, and 15.9913 $\pm$ 0.0036 nm, respectively.

The calibration lines were identified and fit with unweighted Gaussian profiles. The statistical uncertainties, converted to wavelength values, were combined in quadrature with the published wavelength uncertainties to develop weights for the points, and a calibration polynomial was generated. There are a variety of additional potential systematic uncertainties, such as variations in pixel size, pixel response, and drift, so the overall systematic error is estimated by setting $\chi^2 \approx n - N$, where n is the number of calibration points and N is the number of fit parameters in the calibration curve, effectively allowing an average of a one-sigma variation of the residuals [21]. In this way, the systematic uncertainty was determined to be ≈0.0021 nm. The full calibration polynomial was found to be $\lambda[\text{nm}] = 2.7133 \pm 0.00588 + ch \times 0.004542 \pm 1.99 \times 10^{-5} + ch^2 \times 1.345 \times 10^{-6} \pm 2.0 \times 10^{-8} - ch^3 \times 3.858 \times 10^{-11} \pm 5.77 \times 10^{-12}$, where ch is the detector channel. A confidence interval of one standard deviation is generated from the third-order polynomial fit, and all channel-specific errors are derived from the interval. The confidence band, residuals, and approximate spectrometer relative efficiency are shown in figure 1.

3. Analysis and results

The measured spectral lines were fit with unweighted Gaussians, and the statistical uncertainties in the peak fitting were combined with the corresponding confidence intervals
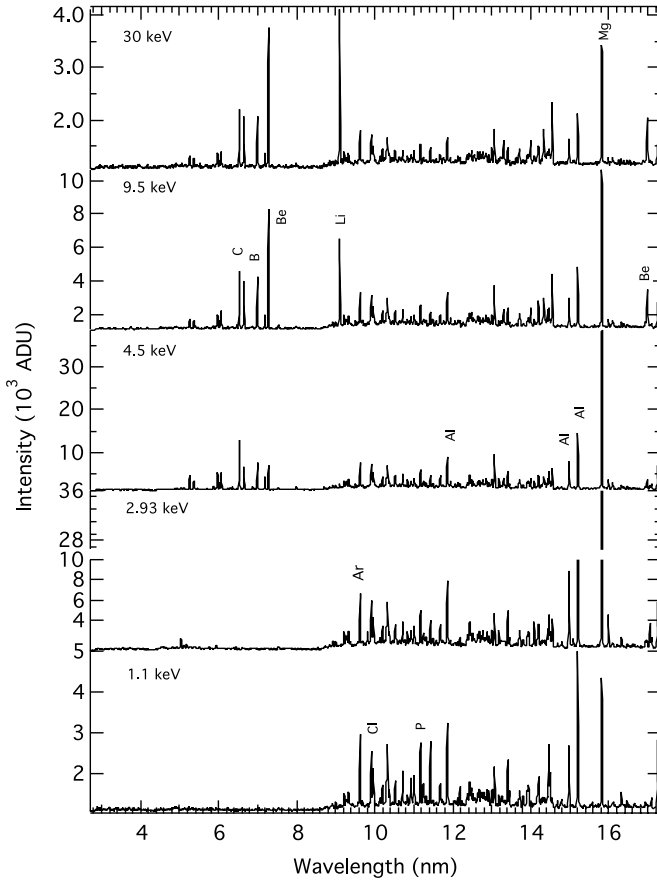
Figure 2. EBIT spectra of krypton (in analogue-to-digital units, ADU, of CCD) at five energies from 1.1 to 30 keV. Select lines are labelled by their isoelectronic sequence.
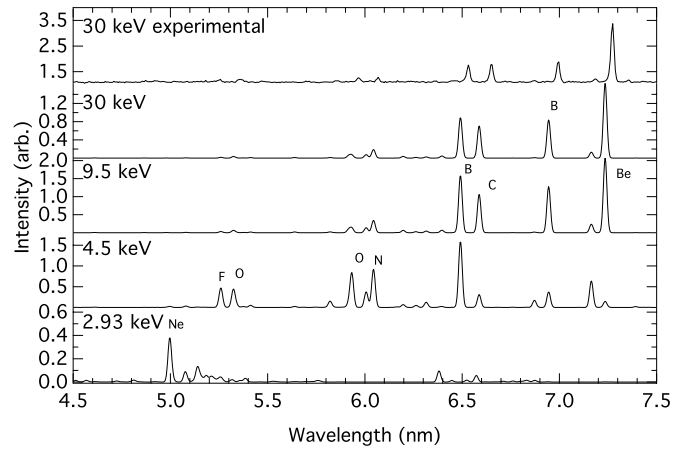

Figure 3. CR simulations between 4.5 and 7.5 nm of the helium-like through neon-like krypton ionization stages. Lines in this region are primarily from $n = 2$ to $n = 2$ transitions. The top trace is from the experimental results at 30 keV, with intensity divided by 1000 to present it on a similar scale, to highlight the comparison of experimental and theoretical line intensities.
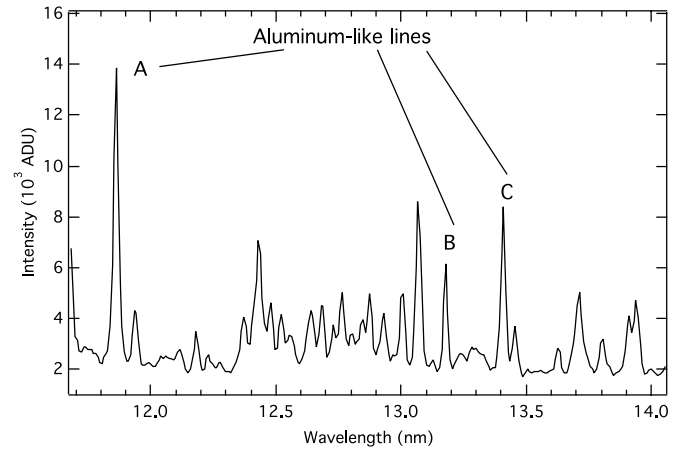

Figure 4. Krypton spectra between 11 and 14 nm. A—11.86 nm $3p_{1/2}–3d_{3/2}$; B—13.18 nm $3p_{3/2}–3d_{5/2}$; C—13.41 nm $3p_{3/2}–3d_{3/2}$.

from the wavelength calibration to generate a combined uncertainty. The estimate of the systematic uncertainty, 0.0021 nm, was then added in quadrature to the previous values to generate the total uncertainty. All uncertainties are given as one standard deviation. Selected krypton spectra are shown in figure 2, with prominent lines indicated by the corresponding isoelectronic sequences. Uncertainties in the wavelengths varied between 0.0024 and 0.0028 nm for most of the measurements.

As mentioned above, the EUV emission was recorded over a wide range of beam energies. The line identifications were based on collisional-radiative (CR) modelling that has been described in detail in previous analyses of EBIT spectra [22–24]. The calculations were performed with the CR code NOMAD [25] using atomic data generated with the Flexible Atomic Code [26]. Simulations at several energies, including spectrometer efficiency effects, are shown in figure 3, focusing on the more dramatically changing spectra in the $n = 2$ to $n = 2$ transitions. Comparison with the experimental spectra of figure 2 shows that our modelling reproduces the observed spectral patterns. These simulations were then used, along with intensity dependence on electron beam energy, to identify the lines of krypton.

The results of the identification for new observations and lines with $\sigma_{new} \leqslant 1.5\sigma_{prev}$, where σ is the uncertainty on the line, are shown in table 1, where we present

the ion charge, isoelectronic sequence, our wavelength measurement and uncertainty, transition information, and previous measurements with uncertainties. Four transitions from F-like and O-like krypton have two measured uncertainties, one of which is below our cut-off. We report these as well, since the larger uncertainty is from the newer measurement which is included in the majority of our results. We also identified the nitrogen-like line at 16.090 nm. The previous identification of this line was described as questionable in its original publication [8].

4. Effect of the M1 transition on allowed transition intensities

Figure 4 shows the measured spectrum between 11 nm and 14 nm at the beam energy of 3.4 keV. This energy is slightly higher than the ionization energy of Ne-like Kr^{26+} (ionization energy = 2928.9 eV), and charge exchange from the input gas will populate the lower ionization stage ions, such as Na-, Mg-, and Al-like Kr. Three spectral lines from Al-like Kr^{23+}

Table 1. Measured wavelengths of highly charged krypton transitions.

Stage	Iso. Seq.	Wavelength (nm)	Uncertainty (nm)	Transition	Previous Experiment (nm)	Previous Uncertainty (nm)	Reference
20+	S	10.5246	0.0026	$3s^2 3p^4 \, ^3P_2 - 3s^2 3p^3 \, (^2D) 3d \, ^3P_1$ [a]			
21+	P	10.9334	0.0026	$3s^2 \, 3p^3 \, ^4S_{3/2} - 3s^2 3p^2 \, (^3P) 3d \, ^4P_{1/2}$			
24+	Mg	16.3252	0.0024	$3s3p \, ^3P_0 - 3p^2 \, ^3P_1$	16.332	0.002	[27]
24+	Mg	17.0970	0.0028	$3s3p \, ^3P_1 - 3p^2 \, ^1D_2$	17.114	0.002	[27]
26+	Ne	5.0403	0.0025	$2s^2 2p^5 3s (3/2,1/2)_1 - 2s2p^6 3s (1/2,1/2)_0$			
26+	Ne	6.4447	0.0025	$2s^2 2p^5 3s (1/2,1/2)_1 - 2s2p^6 3s (1/2,1/2)_0$			
26+	Ne	9.8168	0.0026	$2s^2 2p^5 3s (3/2,1/2)_1 - 2s^2 2p^5 3p (1/2,1/2)_0$			
26+	Ne	17.0507	0.0027	$2s^2 2p^5 3s (1/2,1/2)_1 - 2s^2 2p^5 3p (1/2,1/2)_0$	17.055	0.005	[28]
27+	F	5.2574	0.0025	$2s^2 2p^5 \, ^2P_{3/2} - 2s2p^6 \, ^2S_{1/2}$	5.2594, 5.2584	0.002, 0.0015	[8], [29]
27+	F	6.8705	0.0025	$2s^2 2p^5 \, ^2P_{1/2} - 2s2p^6 \, ^2S_{1/2}$	6.8733, 6.8734	0.003, 0.0015	[8], [29]
28+	O	5.3626	0.0025	$2s^2 2p^4 \, ^3P_1 - 2s2p^5 \, ^3P_1$	5.364, 5.3612	0.003, 0.0015	[8], [29]
28+	O	5.8678	0.0026	$2s^2 2p^4 \, ^3P_0 - 2s2p^5 \, ^3P_1$	5.8700	0.005	[8]
28+	O	5.9708	0.0025	$2s^2 2p^4 \, ^3P_2 - 2s2p^5 \, ^3P_2$	5.9714, 5.9684	0.003, 0.0015	[8], [29]
28+	O	7.9927	0.0025	$2s^2 2p^4 \, ^3P_1 - 2s2p^5 \, ^3P_2$	7.9947	0.003	[8]
28+	O	8.6961	0.0025	$2s^2 2p^4 \, ^1D_2 - 2s2p^5 \, ^3P_2$	8.698	0.004	[8]
29+	N	5.4652	0.0026	$2s^2 2p^3 \, ^2D_{5/2} - 2s2p^4 \, ^2P_{3/2}$	5.4596	0.005	[8]
29+	N	6.0287	0.0025	$2s^2 2p^3 \, ^4S_{3/2} - 2s2p^4 \, ^4P_{1/2}$	6.0332	0.003	[8]
29+	N	6.0689	0.0024	$2s^2 2p^3 \, ^4S_{3/2} - 2s2p^4 \, ^4P_{3/2}$	6.0732	0.0025	[8]
29+	N	6.3619	0.0025	$2s^2 2p^3 \, ^2D_{3/2} - 2s2p^4 \, ^2D_{3/2}$	6.3671	0.003	[8]
29+	N	7.1871	0.0025	$2s^2 2p^3 \, ^4S_{3/2} - 2s2p^4 \, ^4P_{5/2}$	7.1875	0.0025	[8]
29+	N	16.0927	0.0033	$2s^2 2p^3 \, ^4S_{3/2} - 2s2p^4 \, ^2P_{1/2}$	16.090?	0.010	[8]
30+	C	6.5333	0.0025	$2s^2 2p^2 \, ^3P_0 - 2s2p^3 \, ^3D_1$	6.5352	0.002	[8]
30+	C	7.9570	0.0028	$2s^2 2p^2 \, ^3P_1 - 2s2p^3 \, ^3D_2$	7.9557	0.005	[8]
30+	C	9.5047	0.0026	$2s^2 2p^2 \, ^3P_2 - 2s2p^3 \, ^3D_1$	9.5057	0.005	[8]
30+	C	12.8425	0.0027	$2s^2 2p^2 \, ^3P_1 - 2s2p^3 \, ^5S_2$			
31+	B	6.6506	0.0025	$2s^2 2p \, ^2P_{1/2} - 2s^2 2p \, ^2S_{1/2}$	6.6538	0.0025	[8]
31+	B	6.9945	0.0024	$2s^2 2p \, ^2P_{1/2} - 2s2p^2 \, ^2D_{3/2}$	6.9957	0.002	[8]
32+	Be	7.2739	0.0024	$2s^2 \, ^1S_0 - 2s2p \, ^1P_1$	7.2756	0.002	[8]
32+	Be	16.9865	0.0026	$2s^2 \, ^1S_0 - 2s2p \, ^3P_1$	16.9864	0.0025	[8]
33+	Li	9.1032	0.0024	$1s^2 2s \, ^2S_{1/2} - 1s^2 2p \, ^2P_{3/2}$	9.1049 [b]	0.0025	[31]

[a] This level is highly mixed. The leading percentage is only 41%.

[b] Measurement smoothed by isoelectronic sequence are 9.1050 ± 0.001 nm from [30].

can be clearly identified in the spectrum and are marked as A ($3p_{1/2}-3d_{3/2}$ at 11.86 nm), B ($3p_{3/2}-3d_{5/2}$ at 13.18 nm), and C ($3p_{3/2}-3d_{3/2}$ at 13.41 nm). Lines A and C originate from the same upper level $3d_{3/2}$, and therefore in the optically thin plasma of the EBIT their intensity ratio, when defined in terms of energy detected rather than number of photons detected per unit bandwidth, should approximately equal the ratio of the corresponding Einstein coefficients and energies (corrected for the wavelength-dependent spectrometer efficiency). Indeed, the measured ratio of 1.76 is within 16% of the predicted NOMAD value of 2.09. The A:B and C:B line ratios, in turn, cannot be deduced from purely atomic-physics considerations and depend on the population mechanisms for $3d_{3/2}$ and $3d_{5/2}$. If the level populations were proportional to their statistical weights, as one would expect for nearly degenerate levels populated from the ground state via strong optically-allowed excitations, the A:B intensity ratio would be about 0.74, including the energy differences due primarily to the splitting of the lower level. However, the experimental value is approximately 3 at 3.4 keV beam energy.

The reason for this discrepancy can be inferred from the analysis of population channels for the 3d levels (see the Grotrian diagram in figure 5). The population influx to 3d primarily originates in the ground configuration 3p. For
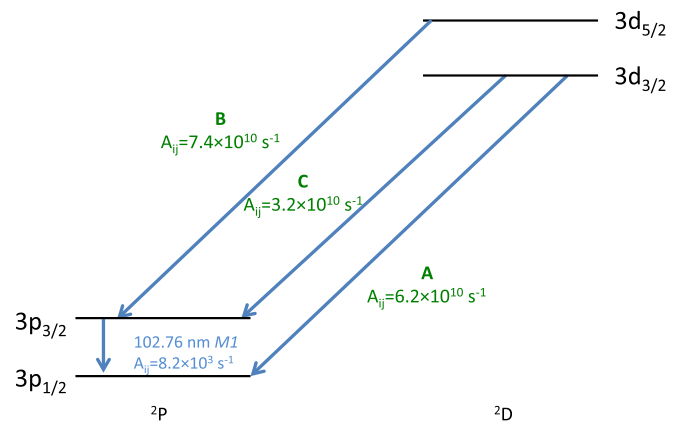

Figure 5. Grotrian diagram of energy levels of interest for the aluminium-like krypton transitions. The calculated transition probabilities are also shown.

the electric dipole allowed 3p–3d excitations, the largest rates are those with $\Delta J = 1$, that is, $3p_{1/2}-3d_{3/2}$ and $3p_{3/2}-3d_{5/2}$. Over a very large range of densities, the former excitation is proportional to electron density, n_e, and is the primary population channel for the $3d_{3/2}$ level. As for the $3d_{5/2}$ level, its population influx is due to a combination of two channels: radiative cascades from the higher levels excited from the $3p_{1/2}$
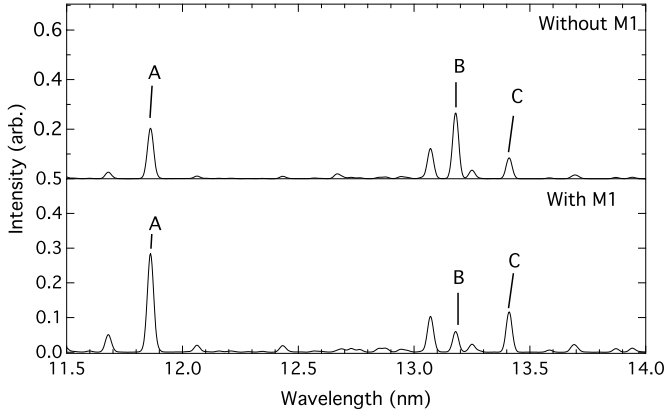
Figure 6. CR modelling of the aluminium-like krypton transitions with and without the M1 transition $3p_{1/2}$–$3p_{3/2}$.

Figure 7. CR modelling of the aluminium-like krypton line ratio (B:A) at five energies in an EBIT. The points mark five of the experimental intensity ratios for the EBIT.

Figure 8. Normalized electron density estimates (black squares) and calculated values using the Al-like line ratio (blue markers) in the EBIT.

ground level (total flux $\propto n_e$) and direct excitation from the $3p_{3/2}$ level. The direct excitation becomes dominant at higher densities when the $3p_{3/2}$ population approaches the density-independent Boltzmann equilibrium with the ground level. However, at low densities the magnetic-dipole (M1) transition $3p_{1/2}$–$3p_{3/2}$ brings these levels close to coronal equilibrium with the $3p_{3/2}$ population $\propto n_e$, so the direct excitation becomes proportional to n_e^2. Such different n_e-dependence of two population mechanisms for the $3d_{5/2}$ level results in a different n_e-dependence of level populations within the 3d configuration and, consequently, density dependence of the line ratios.

The $3p_{1/2}$–$3p_{3/2}$ M1 transition has an expected wavelength of 102.76 nm, well above our region of observation. In order to examine the effect of this magnetic dipole transition, we performed an additional calculation omitting the M1 decay between the 3p levels. Figure 6 has the CR results with and without the M1 transition. For the latter case, the intensity ratios, approximately 0.77:1.00:0.32, approach their statistical (Boltzmann) values. With the M1 line included, the ratios are 4.70:1.00:1.96, qualitatively similar to the experimental measurements.

As explained above, there exists a range of densities where the direct excitation from $3p_{3/2}$ into $3d_{5/2}$ becomes comparable to or stronger than the cascade contribution, and the line ratios B:A and B:C become sensitive to n_e. Shown in figure 7 are the calculated B:A ratios for an EBIT plasma, with a mono-energetic electron beam, at several energies. It is seen that at high and low densities these ratios become n_e-independent, and there is strong electron density dependence between 10^{18} and 10^{20} m^{-3}. From these data, we conclude that the electron densities in these experiments were between 10^{17} m^{-3} and 2×10^{18} m^{-3}, which is in agreement with previous work (see, for example, [32–34], all determined by line ratio measurements).

As an independent check of the measurement, the approximate electron density in the EBIT was estimated for all of the energies by $n_e = I_b/ev_bA_b$, where I_b is the beam current, v_b is the electron beam velocity, and A_b is the beam cross-sectional area. For each energy, the B:A intensity ratio was used to infer the electron density. Since the beam radius is not measured directly, both the estimated and calculated
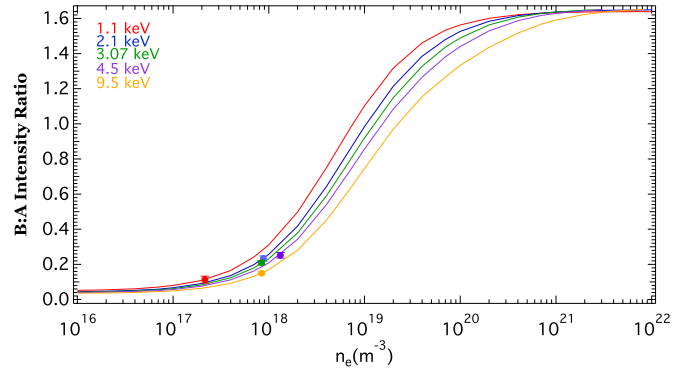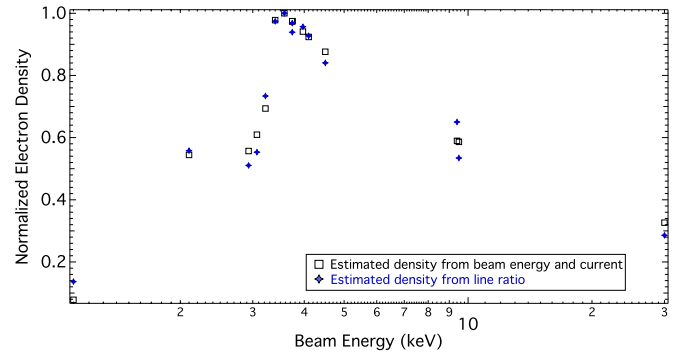
densities are shown normalized to their maximum values as a function of beam energy in figure 8. The decreasing electron density below 3.4 keV is due to the lower beam current in the EBIT at low beam energies, while, above 3.4 keV, the velocity of the electrons increases as a function of beam energy with beam current remaining fairly unchanged. The normalization factor is consistent with the previous diagnostics on the NIST EBIT [35] using neon line ratios and the HULLAC code, assuming a beam radius of 35 microns and a factor of 4.6 effective density reduction due to heating of the ion cloud to significantly larger diameter than that of the electron beam [36]. The gas injection pressure was changed and the EBIT was retuned [16] several times during the experiments which may have resulted in different beam radii and hence explain some of the scatter seen. Overall, the behaviours of the estimated and calculated densities agree, supporting the use of this line ratio for electron density measurements.

CR simulations of these line ratios were also performed with a Maxwellian electron energy distribution approximating the thermalized bulk plasmas of fusion reactors. Figure 9 shows the results of several simulations at various densities at 300, 600, 1000, and 3000 eV. The strong dependence of the line ratio on electron density directly in the region of interest and the fact that the lines are not widely separated in wavelength make this intensity ratio well suited as a diagnostic, particularly during lower-density reactor startup and where imaging UV systems are available, allowing electron density
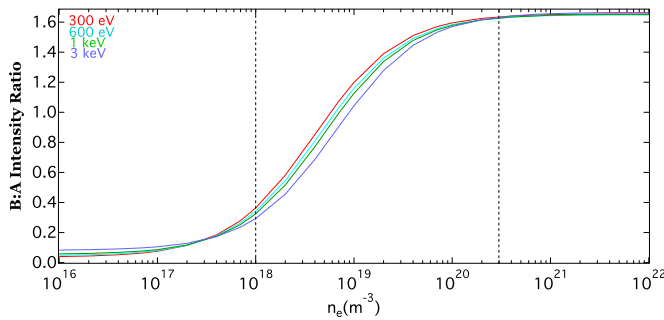
Figure 9. CR modelling of the aluminium-like krypton line ratio (B:A) at various electron densities and temperatures in a Maxwellian plasma. The dashed lines highlight the approximate range of interest for fusion devices.

profiles to be generated by inversion techniques. In current fusion applications, Thomson scattering and reflectometry [37] are used due to their fairly straightforward analysis and high precision. Thomson scattering, however, may not be available on power reactors due to the possibility of the optical components being damaged by the fusion environment [38]. Reflectometry requires high frequency launchers and is incapable of measuring the density on a non-monotonic density profile.

5. Summary and conclusions

EUV spectral lines in highly charged krypton, from lithium-like through sulfur-like ions, have been measured and identified. Wavelength-dependent uncertainties in the calibration curve were taken into account. Six previously unknown transitions were also identified, and a previous tentative transition was confirmed. Twelve of the transitions have improved uncertainties from previous measurements. The $3s^23p$–$3s^23d$ transitions in aluminium-like krypton were found to exhibit ratios that are strongly dependent on electron density in the density regime of interest to fusion. Thus, they were identified as a potential diagnostic of electron density in fusion devices such as ITER.

Acknowledgments

References

 [1] Ikeda K (ed) 2007 *Nucl. Fusion* **47** (special issue)
 [2] Barnsley R, O'Mullane M, Ingesson L C and Malaquias A 2004 *Rev. Sci. Instrum.* **75** 3743
 [3] Beiersdorfer P *et al* 2010 *J. Phys. B: At. Mol. Opt. Phys.* **43** 144008
 [4] Widmann K, Beiersdorfer P, Decaux V and Bitter M 1996 *Phys. Rev.* A **53** 2200
 [5] Widmann K, Beiersdorfer P and Decaux V 1995 *Nucl. Instrum. Methods* B **98** 45
 [6] Kink I *et al* 2001 *Phys. Rev.* E **63** 046409
 [7] Indelicato P, Briand J P, Tavernier M and Liesen D 1986 *Z. Phys. D* **2** 249
 [8] Denne B, Hinnov E, Ramette J and Saoutic B 1989 *Phys. Rev.* A **40** 1488
 [9] Dietrich D D, Stewart R E, Fortner R J and Dukart R J 1986 *Phys. Rev.* A **34** 1912
[10] Chen H, Beiersdorfer P, Fournier K B and Träbert E 2002 *Phys. Rev.* E **65** 056401
[11] Martin S, Denis A, Buchet-Poulizac M C, Buchet J P and Désesquelles J 1990 *Phys. Rev.* A **42** 6570–81
[12] Katai R, Morita S and Goto M 2007 *Plasma Fusion Res.* **2** 006
[13] Serpa F G, Bell E W, Meyer E S, Gillaspy J D and Roberts J R 1997 *Phys. Rev.* A **55** 1832
[14] Chen H, Beiersdorfer P, Harris C L, Utter S B and Wong K L 2001 *Rev. Sci. Instrum.* **72** 983
[15] Saloman E B 2007 *J. Phys. Chem. Ref. Data* **36** 215–386
[16] Gillaspy J, Roberts J, Brown C and Feldman U 1997 *Phys. Scr.* **T71** 99
[17] Blagojevic B *et al* 2005 *Rev. Sci. Instrum.* **76** 083102
[18] Sugar J, Kaufman V, Indelicato P and Rowan W L 1989 *J. Opt. Soc. Am.* B **6** 1437
[19] Sugar J, Kaufman V and Rowan W L 1987 *J. Opt. Soc. Am.* B **4** 1927
[20] Reader J *et al* 1987 *J. Opt. Soc. Am.* B **4** 1821
[21] Hughes I and Hase T 2012 *Measurements and Their Uncertainties* (Oxford: Oxford University Press)
[22] Ralchenko Y *et al* 2008 *J. Phys. B: At. Mol. Opt. Phys.* **41** 021003
[23] Draganić I N *et al* 2011 *J. Phys. B: At. Mol. Opt. Phys.* **44** 025001
[24] Ralchenko Y, Draganić I N, Osin D, Gillaspy J D and Reader J 2011 *Phys. Rev.* A **83** 032517
[25] Ralchenko Y and Maron Y 2001 *J. Quant. Spectrosc. Radiat. Transfer* **71** 609
[26] Gu M F 2008 *Can. J. Phys.* **86** 675
[27] Jupén C, Denne B and Martinson I 1990 *Phys. Scr.* **41** 669
[28] Buchet J *et al* 1988 *Nucl. Instrum. Methods* B **31** 177
[29] Wyart J Fand TFR Group 1985 *Phys. Scr.* **31** 539
[30] Kim Y K, Baik D H, Indelicato P and Desclaux J P 1991 *Phys. Rev.* A **44** 148
[31] Hinnov E and Denne B, The TFTR Operating Team and The JET Operating Team 1989 *Phys. Rev.* A **40** 4357
[32] Silver E *et al* 2000 *Astrophys. J.* **541** 495
[33] Chen H *et al* 2004 *Astrophys. J.* **611** 598
[34] Liang G Y *et al* 2009 *Astrophys. J.* **702** 838
[35] Matranga M *et al* 2003 *Nucl. Instrum. Methods* B **205** 244
[36] Porto J V, Kink I and Gillaspy J D 2000 *Rev. Sci. Instrum.* **71** 3050
[37] Hutchinson I 2002 *Principles of Plasma Diagnostics* 2nd edn (Cambridge: Cambridge University Press)
[38] Yamamoto S and Shikama T 1999 *Proc. SPIE* **3872** 2